Nanoscale Advances

PAPER

View Article Online
View Journal | View Issue

Cite this: *Nanoscale Adv.*, 2019, **1**, 4812

Phage-mimicking antibacterial core–shell nanoparticles†

Juliane Hopf,[a] Margo Waters,[b] Veronica Kalwajtys,[c] Katelyn E. Carothers,[c] Ryan K. Roeder,[bd] Joshua D. Shrout,[a] Shaun W. Lee[c] and Prakash D. Nallathamby *[bde]

The increasing frequency of nosocomial infections caused by antibiotic-resistant microorganisms concurrent with the stagnant discovery of new classes of antibiotics has made the development of new antibacterial agents a critical priority. Our approach is an antibiotic-free strategy drawing inspiration from bacteriophages to combat antibiotic-resistant bacteria. We developed a nanoparticle-based antibacterial system that structurally mimics the protein-turret distribution on the head structure of certain bacteriophages and explored a combination of different materials arranged hierarchically to inhibit bacterial growth and ultimately kill pathogenic bacteria. Here, we describe the synthesis of phage-mimicking antibacterial nanoparticles (ANPs) consisting of silver-coated gold nanospheres distributed randomly on a silica core. The silver-coating was deposited in an anisotropic fashion on the gold nanospheres. Structurally, our nanoparticles mimicked the bacteriophages of the family *Microviridae* by up to 88%. These phage-mimicking ANPs were tested for bactericidal efficacy against four clinically relevant nosocomial pathogens (*Staphylococcus aureus* USA300, *Pseudomonas aeruginosa* FRD1, *Enterococcus faecalis*, and Corynebacterium *striatum*) and for biocompatibility with skin cells. Bacterial growth of all four bacteria was inhibited (21% to 90%) as well as delayed (by up to 5 h). The Gram-positive organisms were shown to be more sensitive to the nanoparticle treatment. Importantly, the phage-mimicking ANPs did not show any significant cytotoxic effects against human skin keratinocytes. Our results indicate the potential for phage-mimicking antimicrobial nanoparticles as a highly effective, alternative antibacterial agent, which may be suitable for co-administration with existing available formulations.

Received 29th July 2019
Accepted 8th October 2019

DOI: 10.1039/c9na00461k

rsc.li/nanoscale-advances

1. Introduction

In 2013, the Centers for Disease Control and Prevention (CDC) published a list of bacteria causing severe human infections and currently presenting the highest risk of developing multi-drug resistance.[1] Most of these bacteria can be found in regular healthcare/hospital settings, spreading *via* surfaces and human contact. The ESKAPE pathogens *Enterococcus faecium*, *Staphylococcus aureus*, *Klebsiella pneumoniae*, *Acinetobacter baumannii*, *Pseudomonas aeruginosa*, and *Enterobacter* species are the leading cause of nosocomial infections (hospital-acquired infections, HAI) world-wide[2] and increasingly exhibit multi-drug resistance to most available classes of antibiotics.[3] More than two-thirds of HAI will turn into chronic, skin, or high-density biofilm infections, which are difficult to treat due to their virulent and adaptive nature.[4]

At the current low rate of antibiotic discovery and development,[5] we may lose the race to contain antibiotic-resistant bacterial strains. Without urgent action, antibiotic-resistant infections will kill more patients per year by 2050 than all cancers combined.[6] Due to the fast emergence and global spread of new resistance, presently treatable infections such as pneumonia, tuberculosis, gonorrhea, and salmonellosis will become harder or near impossible to treat.[7] There is a critical need for broad-spectrum antibacterial agents independent of antibiotics to (a) effectively prevent the progression of antibiotic resistance and (b) provide a necessary alternative to fight infectious diseases.

The use of nanomaterials as alternative antibacterial agents has shown promise owing to their unique physical and chemical properties.[8–11] Nanoparticles (NPs) are below 100 nm in size

[a]*Department of Civil and Environmental Engineering and Earth Sciences, University of Notre Dame, Notre Dame, IN, USA*
[b]*Department of Aerospace and Mechanical Engineering, University of Notre Dame, Notre Dame, IN, USA. E-mail: pnallath@nd.edu; Tel: +1 574 631 7868*
[c]*Department of Biological Sciences, University of Notre Dame, Notre Dame, IN, USA*
[d]*Center for Nanoscience and Technology (NDnano), University of Notre Dame, Notre Dame, IN, USA*
[e]*Center for Advanced Diagnostics and Therapeutics (AD&T), University of Notre Dame, Notre Dame, IN, USA*

† Electronic supplementary information (ESI) available. See DOI: 10.1039/c9na00461k

and exhibit a high surface-to-volume ratio, which enables close interaction with microbial membranes.[12] Specifically, metal and metal oxide NPs have gained attention as a new class of antibacterial agents over the last decade due to their bactericidal properties.[13] NPs containing Ag, Au, Zn, Cu, Ti, Mg, Ni, Ce, Se, Al, Cd, Y, Pd, and super-paramagnetic Fe have been studied in detail.[8,14] Among them, silver NPs showed the most effective, concentration-dependent bactericidal activity against *Escherichia coli* and *Pseudomonas aeruginosa*.[15] Metal and metal oxide NPs inhibit the growth of bacteria (*e.g. Staphylococcus aureus*) by a combination of mechanisms (induction of oxidative stress, cell membrane disruption, and release of metal ions).[16] The advantage of utilizing metal NPs over antibiotics is that the probability of development of bacterial resistance to NPs is less likely.[8] But some bacteria (*Pseudomonas aeruginosa* and *Bacillus subtilis*) have been found to utilize efflux pumps to rid themselves of NPs[17] effectively. Additionally, the high toxicity of these elemental NPs to eukaryotic cells further narrows their therapeutic dosage range.[14]

We hypothesized that the drawbacks associated with antibacterial NPs might be minimized by modularly assembling individually potent antibacterial components into a hierarchical nanostructure accentuating only the desired antibacterial properties of the components while minimizing their toxicity to normal healthy cells. A previous study investigated the shape-dependent antibacterial activity of NPs but used monoelemental (silver) NPs that were not rationally designed to mimic any naturally occurring antibacterial agents.[17] We designed modular NPs that mimic the structure and dimensions of bacteriophages. Phages use structural interactions to infect only bacteria exhibiting the appropriate nanoscale features on the bacterial membrane, and the infectious activity of phages is unaffected by bacterial antibiotic resistance.[18,19] 97% of bacteriophages infecting ESKAPE organisms belong to the *Caudovirales*, an order of tailed bacteriophages (45–170 nm).[20] We synthesized NPs to mimic tailless bacteriophages as a more scalable and reproducible approach compared to mimicking tailed bacteriophages. Therefore, our phage-mimicking ANPs targeted the evolutionarily conserved bacterial membrane with high specificity by structurally mimicking the architecture and function of tailless phages.

Our phage-mimicking ANPs were composed of a silica core studded with smaller, silver-coated gold nanospheres on its surface, mimicking the protein-turret distribution density and high surface-area of icosahedral phage heads (*e.g.*, ΦX174).[21] These phage-mimicking ANPs were designed to (a) electrostatically attract negatively charged bacterial cell membranes with pockets of positive surface charge on the exposed surfaces of the amine-functionalized silica cores, (b) create a high surface area antibacterial silver coating with negligible silver ion leaching compared with current antibacterial formulations, (c) inhibit bacterial growth, (d) be non-toxic to and biocompatible with human cells, and (e) facilitate scalable manufacturing. The synthesis of these phage-mimicking ANPs was confirmed by Transmission Electron Microscopy (TEM) and Inductively Coupled Plasma-Optical Emission Spectrometry (ICP-OES). Bactericidal efficiency was evaluated against four clinically relevant nosocomial pathogens (*Staphylococcus aureus* USA300, *Pseudomonas aeruginosa* FRD1, *Corynebacterium striatum*, and *Enterococcus faecalis*). The ethidium homodimer based dead cell detection assay was used to verify that the phage-mimicking ANPs were noncytotoxic to HaCaT keratinocyte cells (human skin).

2. Methods and materials

2.1 Materials

Staphylococcus aureus USA300;[22] *Corynebacterium striatum*;[23,24] *Enterococcus faecalis*;[24,25] *Pseudomonas aeruginosa* FRD1;[26] 200 proof ethanol (VWR); 20% w/v ammonium hydroxide (NH_4OH; BDH); tetraethyl orthosilicate (TEOS; Sigma Aldrich, 99% GC grade); 3-aminopropyltriethoxysilane (APTES; Sigma Aldrich, 99%); sodium hydroxide (NaOH; Sigma Aldrich, >97%); sodium citrate dihydrate ($C_6H_5Na_3O_7 \cdot 2H_2O$; Sigma Aldrich, >99%); tetrakis(hydroxymethyl)phosphonium chloride (80% purity) (THPC; Sigma Aldrich, 80% in water); gold chloride (anhydrous; Sigma Aldrich); silver nitrate ($AgNO_3$; Sigma Aldrich, 99% ACS grade); hydroquinone (Sigma Aldrich, >99% reagent grade); deionized water (DI water); 16% w/v paraformaldehyde (Beantown Chemical); Dulbecco's Modified Eagle's Medium (DMEM; Gibco); heat-inactivated fetal bovine serum (FBS); phosphate buffered saline (pH 7.4; Gibco); ethidium homodimer (Molecular Probes); 0.1% (w/v) saponin (Sigma).

2.2 Nanoparticle synthesis

Silica cores were synthesized by a sol–gel method (Stöber process). Alkaline reduction was performed at room temperature to synthesize gold nanospheres.[27] In a multistep process derived from established chemistry, the gold nanospheres were immobilized on the silica cores[28] and coated with a thin layer of silver.[29] To investigate the influence of nanoparticle size on bacterial growth, two sizes of silica cores – small (45 nm) and large (130 nm) – were produced. Additionally, the concentration of silver coating the gold nanospheres was also varied, including a low silver (LS), medium silver (MS), and high silver (HS) concentration. In total, 10 nanoparticle variations were synthesized and characterized: 45 nm SiO_2, 45 nm SiO_2@Au, 45 nm SiO_2@Au@Ag LS, 45 nm SiO_2@Au@Ag MS, 45 nm SiO_2@Au@Ag HS, 130 nm SiO_2, 130 nm SiO_2@Au, 130 nm SiO_2@Au@Ag LS, 130 nm SiO_2@Au@Ag MS, and 130 nm SiO_2@Au@Ag HS. The process of synthesizing the phage-mimicking nanoparticles is illustrated in Fig. 1.

2.2.1 Silica core synthesis and silanization. The Stöber method of hydrolysis and condensation of TEOS was utilized to synthesize monodispersed silica-cores with diameters of 45 and 130 nm by varying the amount of ethanol, water, NH_4OH solution, TEOS, and the material of the reaction vessel. For the 45 nm silica particles, 30 ml ethanol, 6 ml of DI water, 1.125 ml TEOS, and 1.8 ml of 20% w/v NH_4OH in water were stirred in a covered glass reactor overnight (minimum of 8 h). The 130 nm silica particles were synthesized in a Teflon reactor by first stirring 5 ml ethanol with 1.3 ml TEOS and then adding a mixture of 22 ml ethanol and 7 ml of 20% w/v NH_4OH in water

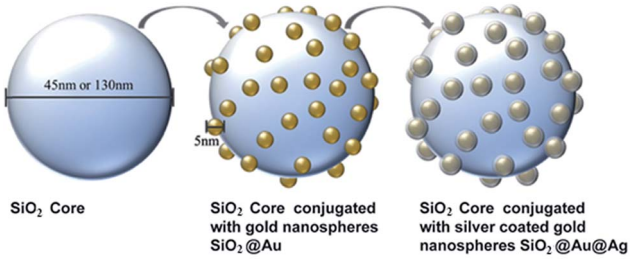

Fig. 1 Schematic illustration of the three major steps for synthesizing phage-mimicking silica-based ANPs. First, 45 nm and 130 nm SiO_2 nanoparticle cores were synthesized, followed by the conjugation of gold nanospheres to the cores. Finally, three different concentrations of silver were added as a coating over the gold nanosphere surface to produce low silver (LS), medium silver (MS), and high silver (HS) variants. The schematic is not to scale.

into the Teflon beaker. The covered Teflon reactor was set to stir overnight (minimum of 8 h) at room temperature. Both SiO_2 core size solutions were centrifuged at 9000 rcf for 30 min at room temperature to allow the synthesized nanoparticles to settle down and separate from the supernatant. The nanoparticle pellets were washed, sonicated (20 s at 40% amplitude), and rinsed with 10 ml ethanol twice by centrifugation.

To adsorb the gold nanospheres on the SiO_2 cores, the solutions of silica cores (45 nm and 130 nm) were amine-functionalized by stirring overnight with additional 15 ml ethanol, 5 ml DI water, and 1 ml APTES. 45 nm and 130 nm SiO_2–APTES cores were centrifuged at 9000 rcf for 30 min at room temperature and separated from the supernatant. The amine-functionalized nanoparticle pellets were washed, sonicated (20 s at 40% amplitude), and rinsed with 10 ml ethanol twice by centrifugation at 9000 rcf. After the last rinse, the centrifuged pellet was resuspended in 10 ml DI water and sonicated (20 s at 40% amplitude).

2.2.2 Gold nanosphere synthesis and conjugation to silica cores. Gold nanospheres with a size of ~5 nm were synthesized using a modified version of previously established procedures.[19] 40.4 ml DI water, 400 μL NaOH (1 M), 3 ml sodium citrate dihydrate (68 nM), and 1 ml THPC (85 mM) were stirred for 10 minutes at room temperature. After that, 2 ml gold chloride (25 mM) was added and stirred overnight (minimum of 8 h) in the dark. In a ratio of 1 : 2 (v/v), the gold nanosphere solution was mixed into the SiO_2–APTES core solutions and stirred (minimum of 8 h) in the dark. Afterward, both SiO_2@Au nanoparticle solutions were centrifuged at 9000 rcf for 15 min at room temperature, followed by two cycles of washing–sonication–centrifugation in 10 ml of DI water.

2.2.3 Variable silver coating of gold nanospheres. Finally, three different concentrations of silver (low, medium, and high) were alloyed with the surface of the gold nanospheres previously adsorbed to the silica cores. The SiO_2@Au nanoparticle solutions were mixed with 10 mM $AgNO_3$ and 10 mM freshly prepared hydroquinone in the proportions shown in Table 1.

After mixing, the solutions were stirred for one hour for the low silver (LS) phage-mimicking ANPs and overnight for the medium silver (MS) and high silver (HS) phage-mimicking ANPs. The silver coating reaction was stopped by centrifugation and discarding of the supernatant. The resulting SiO_2@Au@Ag nanoparticle pellets were washed and centrifuged two additional times in 10 ml DI water. All SiO_2@Au@Ag nanoparticle solutions were stored in the dark until they were used for characterization and bacterial testing.

2.3 Nanoparticle characterization

2.3.1 TEM investigation. Two SiO_2@Au@Ag nanoparticle samples (45 nm SiO_2@Au@Ag HS and 130 nm SiO_2@Au@Ag HS) were prepared for TEM investigation by drop coating the dispersed sample onto a 200-mesh copper grid coated with an amorphous carbon film. TEM images of the phage-mimicking nanoparticles were obtained on a JEOL 2011 microscope at an acceleration voltage of 200 kV. Image analysis was carried out with ImageJ. The diameters of 287 gold nanospheres, 314 small SiO_2 nanoparticle cores, and 75 big SiO_2 nanoparticle cores were measured from over 60 selected images. From the averaged diameter of all these three main components, the surface area of silver and the surface coverage of the silica cores by the silver-coated gold nanospheres were calculated. Additionally, the distance between the silver-coated gold nanospheres was quantified for the small (45 nm) and large (130 nm) phage-mimicking ANPs by measuring the distance between a gold-nanosphere and its three closest neighbors. This information is necessary to fully compare the phage-mimicking ANPs to the actual dimensions of real bacteriophages.

2.3.2 Inductively coupled plasma-optical emission spectroscopy (ICP-OES). Elemental analysis of silver and gold was performed using ICP-OES with a PerkinElmer Optima 8000. Emission spectra for Au and Ag were collected at 267.595 nm and 328.068 nm, respectively. Emission spectra for yttrium (Y), an internal standard, were collected at 371.029 nm. 0, 0.2, 1, 2,

Table 1 Composition of alloy solutions used to create three variants of silver coating on the gold nanospheres previously conjugated to the silica cores

Phage-mimicking ANPs	SiO_2@Au nanoparticle solution (45 and 130 nm) 1% w/v SiO_2	Silver nitrate solution (10 mM)	Hydroquinone solution (10 mM)
Low silver (LS)	30 ml	3 ml	0.3375 ml
Medium silver (MS)	30 ml	3 ml	1.8 ml
High silver (HS)	30 ml	7.2 ml	5.76 ml

5, and 10 ppm gold and silver standards in 5% nitric acid were prepared from commercially available 1000 ppm Au and Ag(II) standard solutions. The average correlation coefficient (R^2) of the calibration curves was 0.9999 (Au) and 0.9986 (Ag).

2.4 Biocidal activity against planktonic bacteria

All ten synthesized nanoparticle variations, SiO_2, SiO_2@Au, SiO_2@Au@Ag LS (low silver), SiO_2@Au@Ag MS (medium silver), and SiO_2@Au@Ag HS (high silver) in both sizes (45 and 130 nm), were screened against four clinically relevant nosocomial bacterial strains/pathogens (*Staphylococcus aureus* USA300, *Pseudomonas aeruginosa* FRD1, *Corynebacterium striatum*, and *Enterococcus faecalis*). Glycerol stocks of all four strains were kept at −80 °C, and each week fresh lysogeny broth agar (LB) plates were streaked with each strain. To adapt the strains to a planktonic lifestyle, a single colony from each LB plate was transferred to a 6 ml LB growth tube and grown at 37 °C under continuous shaking for approximately 12 h to produce a pre-culture before each plate reader run. Additionally, this preparation resulted in very consistent bacterial cell counts (*Staphylococcus aureus* USA300: 5×10^9 CFU ml^{-1}; *Pseudomonas aeruginosa* FRD1: 2×10^9 CFU ml^{-1}; *Corynebacterium striatum*: 2×10^9 CFU ml^{-1}; *Enterococcus faecalis*: 6×10^8 CFU ml^{-1}) used to inoculate the experimental runs. The biocidal activity experiments were run with at least four replicates for each NP variation, the background (LB), and the control (strain growing in LB only) in a 96 well plate. All single tests were premixed in a small growth tube containing 2 ml with subsequent additions of 10 μl bacterial inoculate from the pre-culture and different concentrations of the three different silver variant phage-mimicking ANPs. These premixed samples were thoroughly mixed, and 200 μl was pipetted into each well of a sterile 96 well plate. With shaking, the 96-well plate containing all biocidal activity tests was incubated at 37 °C for 24 h with OD_{600} measurements taken every 10 min. The resulting growth curves were corrected with the LB media background measurements.

2.5 Dark-field imaging

S. aureus USA300 isolates (methicillin-resistant, community-associated) are continuously evolving their resistance profiles.[22] Therefore, the interaction of this pathogen with phage-mimicking ANPs was directly observed by dark-field microscopy. *S. aureus* USA300 cells were incubated for 24 h with different concentrations of SiO_2@Au@Ag HS, aspirated from their individual wells (96 well plate) and collected by centrifugation for 10 min at room temperature. After removal of the supernatant, 4% paraformaldehyde (w/v in PBS) was added to the residual cell pellet. To ensure that all bacterial cells are fixed, the sample was vortexed for 1 min and then incubated for 30 min at room temperature. The fixing agent was removed by centrifugation, discarding the supernatant, and two consecutive rinses with PBS. Sample solutions were stored in PBS at 4 °C until further investigation.

Fixed *S. aureus* USA300 cells were imaged using a dark-field optical microscope (DFOM) equipped with a QIClick CCD camera, a QImaging 01-Rgb-Hm-S-Ir high-resolution color filter, a dark-field condenser (oil 1.43–1.20, Nikon), and a 100× objective (Nikon Plan Fluor 100× oil, iris, SL NA 0.5–1.3, WD 0.20 mm) with a depth of field (focus) of 190 nm. Typically, 10 μl of the samples were added to 1 mm thick glass slides and covered with a #1 glass coverslip. Color images were 12 bit, 2 × 2 binned, and had exposure times between 100 and 200 ms. Images were analysed using ImageJ.

2.6 Biocompatibility testing

For all biocompatibility studies, HaCaT human epithelial keratinocytes were used, maintained in Dulbecco's Modified Eagle's Medium (DMEM) supplemented with 10% heat-inactivated fetal bovine serum (FBS), and incubated at 37 °C with 5% CO_2 in 100 mm culture dishes. The ethidium homodimer cell death assay[30] was used to determine the cytotoxicity of all ten synthesized nanoparticle variations (SiO_2, SiO_2@Au, SiO_2@Au@Ag LS (low silver), SiO_2@Au@Ag MS (medium silver), and SiO_2@Au@Ag HS (high silver), both sizes (45 and 130 nm)). For this assay, HaCaT cells were grown to approximately 75–80% confluency in 24 well tissue culture plates with DMEM. HaCaT cells were between passage numbers 16–25 when cultured from liquid nitrogen storage. Before the nanoparticle treatment, DMEM was aspirated from the wells, and the cells were washed with PBS. Then PBS was aspirated from the wells and the nanoparticle solution (in DMEM) was added in two concentrations (LC, low concentration = approximately 6.99×10^{11} particles per ml of 45 nm phage-mimicking ANPs and 1.09×10^{11} particles per ml of 130 nm phage-mimicking ANPs; HC, high concentration = approximately 1.40×10^{12} particles per ml of 45 nm phage-mimicking ANPs and 2.19×10^{11} particles per ml of 130 nm phage-mimicking ANPs). Cells were then incubated for 16 h at 37 °C with 5% CO_2. After incubation, DMEM was aspirated, and cells were washed with PBS to remove the free-floating nanoparticles. 4 μM ethidium homodimer in PBS was added, and cells were incubated for 30 min in the cell culture incubator. The level of fluorescence was determined using a plate reader set to 528 nm excitation and 617 nm emission with a cut-off value of 590 nm. The percentage of dead cells was determined by adding 0.1% (w/v) saponin to each well following the initial reading in order to permeabilize all cells and incubating the plate for an additional 20 min at room temperature followed by shaking the plate on an orbital shaker before reading the plate a second time at the same settings. Percent membrane permeabilization was calculated by dividing the fluorescence values with intact cells by the fluorescence values after cell disruption by saponification. Each treatment condition was performed in triplicate, with the average cell viability (as a percent of the control) plus standard deviation of all conditions plotted together for comparison. Significance was determined by ANOVA and the *t*-test (one tail and two tail).

3. Results and discussion

3.1 Structural similarity of phage-mimicking antibacterial nanoparticles to bacteriophages

For a visual comparison, Fig. 2A and B show the structure of a tailless phage (the example of bacteriophage ΦX174) that

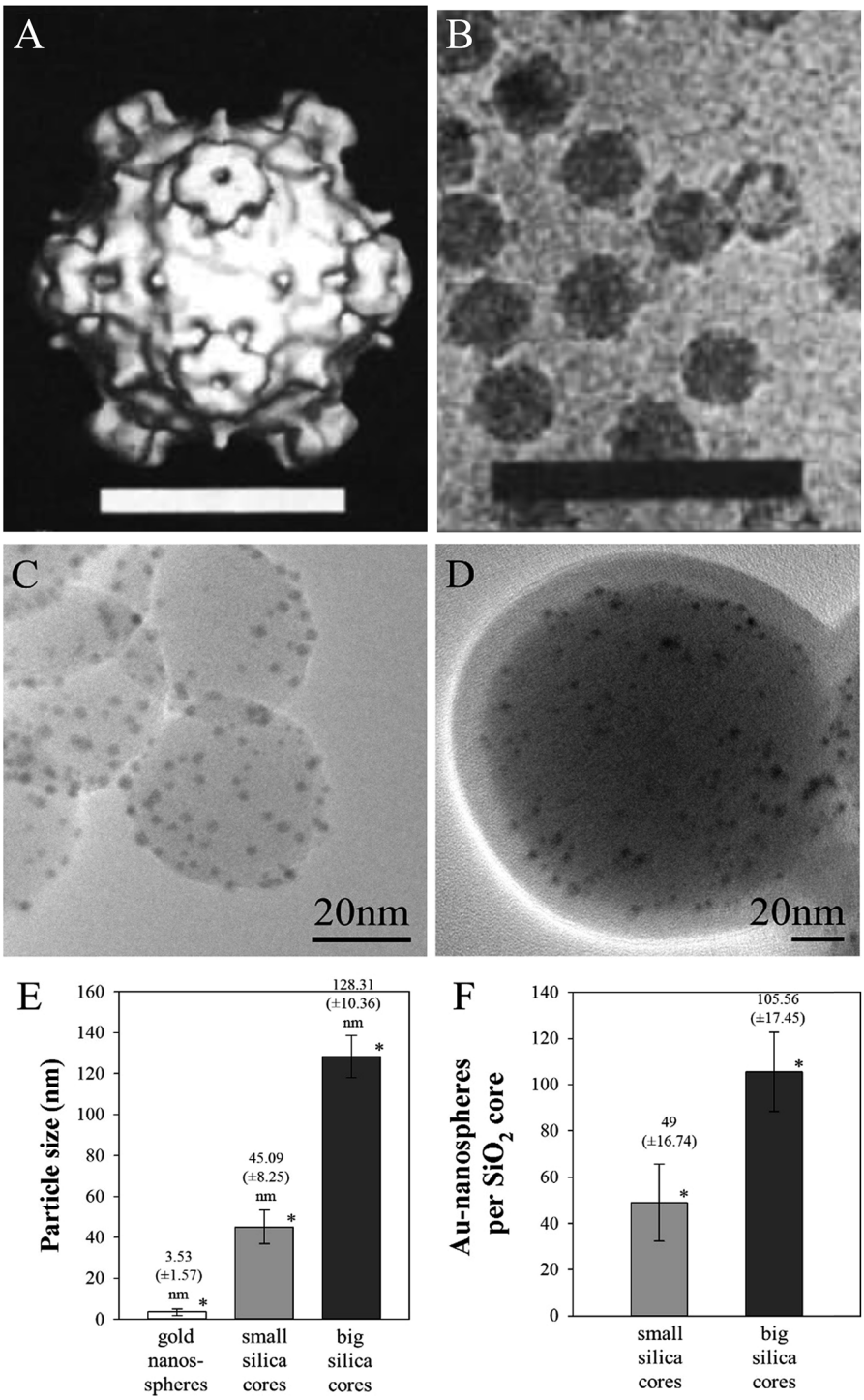

Fig. 2 The procapsid particles of bacteriophage ΦX174 presented as (A) a surface-rendered image (scale bar: 20 nm) from (B) cryo-electron microscopy images (HRTEM) (scale bar: 100 nm) (reproduced with permission).[70] SiO_2@Au@Ag NPs with (C) small 45 nm and (D) large 130 nm core sizes are shown with the example of the high silver coating on the gold nanospheres. (E) The mean diameter of the gold nanospheres and SiO_2 cores. (F) The number of gold nanospheres on silica cores. *$P \leq 0.01$ (*t*- and *f*-test).

acted as a template for the design of our antibacterial nanoparticles.[31] TEM image analysis revealed that the small and large SiO_2 cores had diameters of approximately 45 ± 8.25 nm and 130 ± 10.36 nm, respectively, and were covered with 3.5 ± 1.57 nm gold-nanospheres (Fig. 2C–E). The amount of gold nanospheres covering the phage-mimicking ANPs varied from ~50 for the 45 nm core size to ~105 for the larger 130 nm SiO_2 core (Fig. 2F). For a more detailed comparison of the phage-mimicking ANPs with the head structure of tailed and tailless phages, Table 2 analyzes 9 phages and lists the number of

Table 2 Structural comparison of the heads of tailed (P68, phi8812, and φKZ) and tailless bacteriophages (ΦX174, PM2, PRD1, STIV, and SpV4) with small (45 nm) and large (130 nm) phage-mimicking ANPs with respect to the number of protein turrets per capsid (number of gold nanospheres per silica core), capsid diameter (silica core diameter), interspacing between protein turrets on the capsid (interspacing between gold nanospheres on the silica core), surface area of the capsid (surface area of the silica core), and surface density of protein turrets (surface density of gold nanospheres). The surface area of phage-heads was calculated for the icosahedral shape

Tailed bacteriophage	Number of protein turrets/capsid	Capsid diameter (nm)	Interspacing between protein turrets on capsid (nm)	Surface area of capsid (nm^2)	Surface density of protein turrets (nm^{-2})
P68	12	48	11.33	5191	0.0023
phi812	12	90	29.58	24 916	0.0005
φKZ	12	145	59.80	46 407	0.0003
Tailless bacteriophage	**Number of protein turrets/capsid**	**Capsid diameter (nm)**	**Interspacing between protein turrets on capsid (nm)**	**Surface area of capsid (nm^2)**	**Surface density of protein turrets (nm^{-2})**
ΦX174	12	28	8.28	3068	0.0039
PM2	12	59	28.61	10 120	0.0012
PRD1	12	64	17.32	11 898	0.0010
STIV	12	70	27.25	14 496	0.0008
SH1	12	82	36.44	15 827	0.0008
SpV4	18	31	9.31	2635	0.0068
Phage-mimicking ANPs	**Number of Au nanospheres/silica core**	**Silica core diameter (nm)**	**Interspacing between Au nanospheres on silica core (nm)**	**Surface area of silica core (nm^2)**	**Surface density of Au nanospheres (nm^{-2})**
Small (45 nm)	49	45	2.02	6362	0.0077
Large (130 nm)	106	130	9.87	53 093	0.0020

protein-turrets on the viral capsid of the phages, their capsid diameter, the interspacing between the protein turrets, the surface area of the capsid, and the surface density of the protein turrets. The surface area of the capsid was calculated for the icosahedral shape. Cryo-electron microscopy imaging data from the protein database (PDB) was used to determine the dimensions of the individual capsid proteins.

In general, the size of the smaller phage-mimicking ANPs (45 nm) relates better to the capsid sizes of tailless bacteriophages than that of the larger 130 nm phage-mimicking ANPs. Both the 45 nm and 130 nm core sizes carry more gold nanospheres per unit area in comparison to the number of protein turrets on the heads of the bacteriophage's capsids (~4× and 8× higher, respectively). Regardless, the 2.02 nm interspacing between the gold nanospheres of the small 45 nm phage-mimicking ANPs is at least 4× smaller than the geometrically consistent distance between the protein-turrets covering the surface of the phage capsids. The gold nanosphere interspacing of 9.87 nm on the larger 130 nm phage-mimicking ANPs, on the other hand, is comparable to the protein turret interspacing found on the smaller bacteriophages P68, ΦX174, and SpV4 (11.33 nm, 8.28 nm, and 9.31 nm) (Table 2).[32–34]

Interestingly, the bacteriophage SpV4 possesses a surface density of protein turrets (0.0068 nm^{-2}) that is 88% similar to the surface density of gold nanospheres (0.0077 nm^{-2}) on small 45 nm phage-mimicking ANPs.[33] The SpV4 bacteriophage belongs to the viral family of *Microviridae* which are small (25–27 nm), tailless bacteriophages.[35] One genus of this family is named *Chlamydiamicrovirus* and as the name suggests it infects various species of the obligate intracellular and pathogenic *Chlamydia*.[36] Bacteriophages of the genus *Chlamydiamicrovirus* are known to initiate infection of the bacterial host cell by pilus-mediated adsorption, which is dependent on the external bacteriophage structure as well as the host cell receptors.[37–40] Additionally, the surface density of protein turrets on the *Staphylococcus aureus* infecting bacteriophage P68 (0.0023 nm^{-2}) is 85% similar to the surface density of gold nanospheres on the larger 130 nm phage-mimicking ANPs (0.0020 nm^{-2}).[32] Thus, the surface density of silver-coated gold nanospheres on the silica cores of both phage-mimicking ANP sizes is closely related to the surface density of protein turrets of pathogen-infecting bacteriophages which is indicative of the phage structure mimicking properties of our phage-mimicking ANPs. Importantly, in our manufacturing technique, we used redox plating to alloy silver[41] with randomly distributed gold nanospheres already immobilized on silica cores resulting in an anisotropic silver shell on the gold nanospheres. Our synthesis protocol led to robust retention of the phage-mimicking structure under physiological conditions as opposed to techniques that employ only electrostatic immobilization of nanospheres on silica cores (Table 3).

3.2 Antibacterial activity of phage-mimicking nanoparticles against four nosocomial strains

3.2.1 *Staphylococcus aureus* USA300. *Staphylococcus aureus* USA300 is a methicillin-resistant (MRSA) strain predominantly associated with skin and soft tissue infections, but has also

Table 3 Theoretical correlation of the contact surface of silver-coated gold nanospheres on the surface of the SiO_2 cores to the surface area of silver coating. Schematics are not to scale

	Single point of contact on silica cores by immobilizing pre-synthesized Au@Ag core–shell NPs (nm^2)	Robust hemispherical contact on silica cores by anisotropic plating of Ag on immobilized Au nanospheres (nm^2)
(a) Schematic	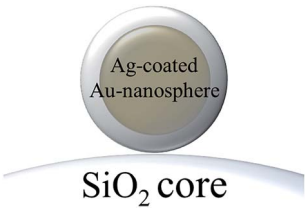	
(b) Surface area of the interface	0	≤9.81
(c) Surface area of silver	≥39.24	≤19.62

been recovered from severe cases of invasive disease including bacteremia, endocarditis, necrotizing pneumonia, and osteomyelitis.[22] Fig. 3 gives a complete overview of the antibacterial activity of all silver-containing phage-mimicking ANPs *versus* *Staphylococcus aureus* USA300, indicating that with increasing silver coating, the phage-mimicking ANPs show enhanced growth inhibition as well as lower final bacterial counts. The highest silver concentration used in this experiment of approximately 95 μg ml^{-1} on 130 nm HS phage-mimicking ANPs (factoring in the dilution factor) was quite effective in inhibiting the growth of *Staphylococcus aureus* USA300. It is well documented in the literature that silver nanoparticles (AgNPs) inhibit the growth and reproduction of bacterial cells treated with different concentrations of unmodified ~18.17 nm AgNPs.[41] The bacterial growth of *Staphylococcus aureus* and *Escherichia coli* cells treated with 25 μg ml^{-1} AgNPs was significantly lower than that of cells in the control group, whereas the growth of bacterial cells treated with 50 and 100 μg ml^{-1} AgNPs was completely inhibited.[42,43] Tamboli and Lee[44] observed significant growth inhibition when incubating *Staphylococcus aureus* with 100 μg ml^{-1} of larger ~30 nm AgNPs, which interestingly falls in line with the highest silver concentration (95 μg ml^{-1}) measured on our nanoparticles. The added advantage of our phage-mimicking antibacterial nanoparticles is that silver is alloyed with gold (minimum Au : Ag = 70 : 30) (Table 4) which will result in <1 μg ml^{-1} silver ions leaching into solution for every 100 μg ml^{-1} 70 : 30 Au : Ag nanoalloy used.[45] In fact using ICP-OES we were not able to detect any Ag ions in the

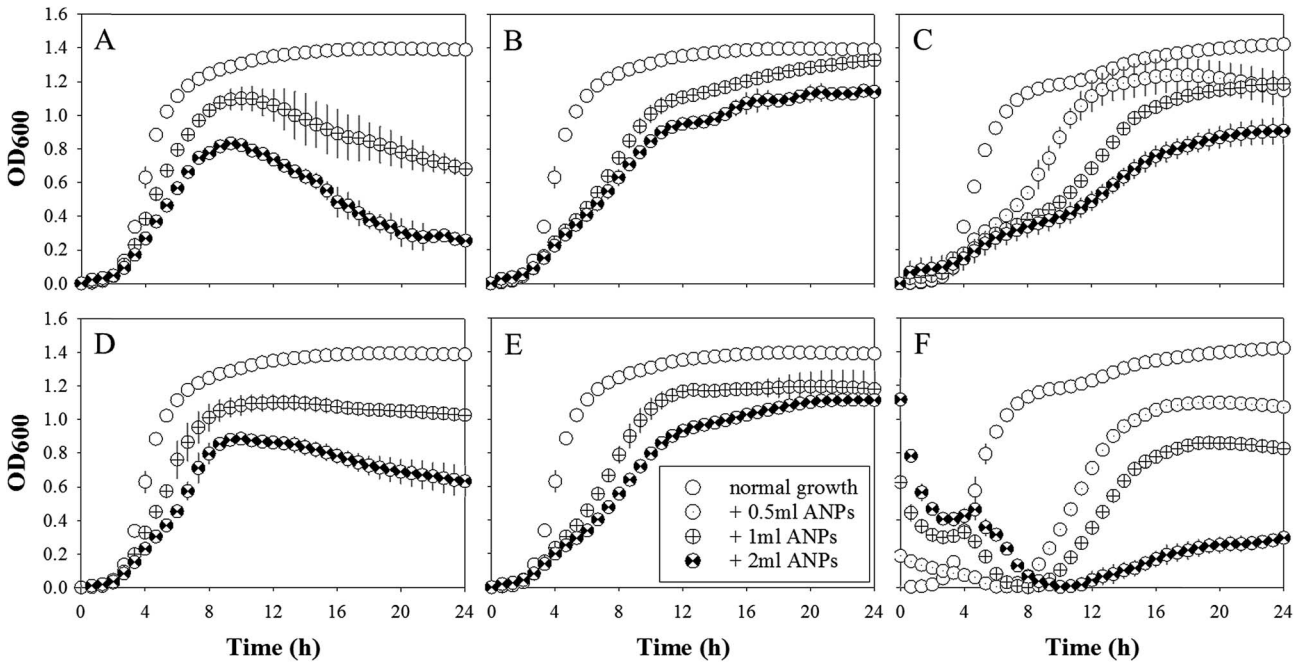

Fig. 3 Growth of *Staphylococcus aureus* USA300 in the presence of (A–C) small 45 nm and (D–F) large 130 nm phage-mimicking ANPs with various silver coatings containing (A and D) low, (B and E) medium, and (C and F) high silver concentrations.

Table 4 Gold and silver concentrations in the phage-mimicking ANP stock solution used for bactericidal and biocompatibility testing

Phage-mimicking ANPs	Gold concentration, $\mu g\ ml^{-1}$ (±SD)	Silver concentration, $\mu g\ ml^{-1}$ (±SD)
45 nm LS	637.61 (±52.91)	17.64 (±9.77)
130 nm LS	679.59 (±51.04)	26.62 (±13.57)
45 nm MS	624.86 (±39.65)	92.15 (±58.60)
130 nm MS	652.48 (±67.73)	141.63 (±81.42)
45 nm HS	665.21 (±66.93)	123.25 (±87.91)
130 nm HS	635.32 (±50.35)	189.22 (±122.13)

supernatant of phage-mimicking ANPs exposed to bacterial cell culture conditions. The negligible leaching of silver ions from our phage-mimicking ANPs will lead to less off-target toxicity. The unique architecture of our phage-mimicking nanoparticles will achieve similar (if not better) results than silver nanoparticles in actively inhibiting the growth of *Staphylococcus aureus* USA300.

3.2.2 *Pseudomonas aeruginosa* FRD1. *Pseudomonas aeruginosa* FRD1 is a mucoid strain originally isolated from a chronically infected cystic fibrosis patient with the ability to overproduce exopolymeric alginates, favorable for biofilm formation.[26,46] As the only Gram-negative strain in our

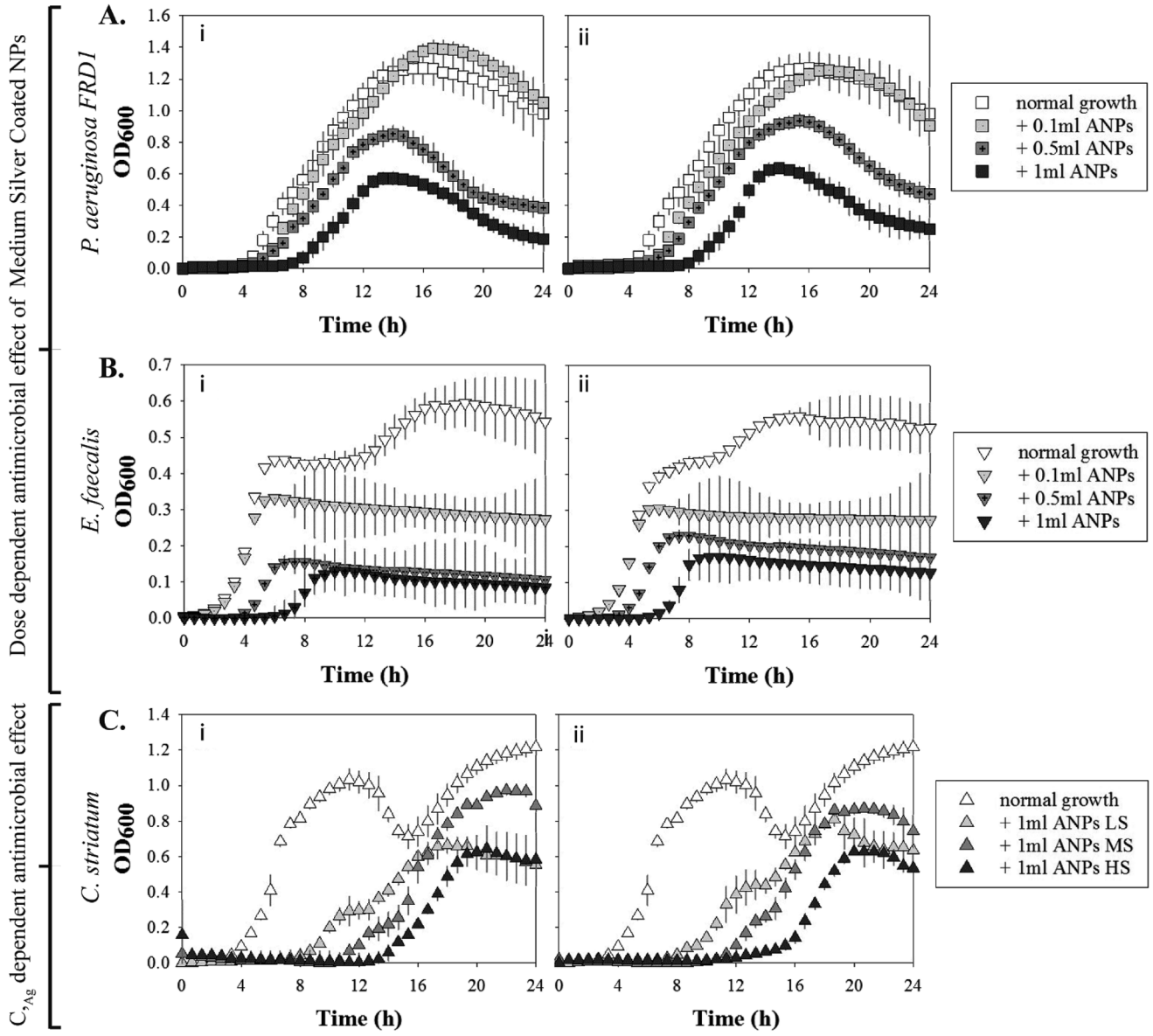

Fig. 4 *P. aeruginosa* FRD1 and *E. faecalis* exhibited dose-dependent log phase inhibition when treated with medium silver-coated NPs. Growth of *P. aeruginosa* FRD1 in the presence of (A(i)) small 45 nm and (A(ii)) large 130 nm NPs with the medium silver-coating in three different dosages (0.1, 0.5, and 1 ml). Growth of *E. faecalis* in the presence of (B(i)) small 45 nm and (B(ii)) large 130 nm NPs with the medium silver coating in three different dosages (0.1, 0.5, and 1 ml). *C. striatum* exhibited a silver coverage dependent retardation of log-phase initiation for a given dose (*e.g.*, 1 ml). Growth of *C. striatum* in the presence of a 1 ml dose of either (C(i)) small 45 nm or (C(ii)) large 130 nm phage-mimicking ANPs with silver coatings varied from low (LS) to medium (MS) to high (HS).

experiments, *Pseudomonas aeruginosa* FRD1 also presented a dose-dependent sensitivity towards higher concentrations of phage-mimicking ANPs with the medium silver coating (Fig. 4A). 1 ml of an MS phage-mimicking ANP sample (45 nm or 130 nm) contains approximately 31–47 μg ml^{-1} silver (considering dilution). Non-mucoid strains of *Pseudomonas aeruginosa* have been observed to be growth inhibited by around 10 μg ml^{-1} AgNPs.[47] But for the mucoid strain *P. aeruginosa* FRD1 incubated with the phage-mimicking ANPs, we observed that the culture wells presented a mucoidal substance on the well bottom. The production of alginates (the main component of mucus) by *Pseudomonas aeruginosa* FRD1 might be indicative of the defense mechanisms of the bacterium to protect the bacterial cell wall from direct contact with the phage-mimicking ANPs.

3.2.3 *Enterococcus faecalis*. *Enterococcus faecalis* can cause endocarditis, septicemia, urinary tract infections, and meningitis.[24,25] As an opportunistic nosocomial pathogen representing a high risk for immunocompromised patients in the clinical environment, *Enterococcus faecalis* was observed to be the most sensitive to the phage-mimicking ANP treatment. MS phage-mimicking ANPs containing 31–47 μg ml^{-1} silver (factoring dilution) inhibited the growth of *Enterococcus faecalis* and inhibited the maximum cell count 3-fold in comparison to the normal/healthy growth of the culture (Fig. 4B). Krishnan *et al.*[48] reported an inhibitory effect of 5 mg ml^{-1} AgNPs (45–50 nm) towards *Enterococcus faecalis*, which was 100-fold higher than that of the antibacterial Ag concentrations on our phage-mimicking ANPs.

3.2.4 *Corynebacterium striatum*. *Corynebacterium striatum* is often resistant to several antibiotics, and it is associated with wound infections, pneumonia, and meningitis.[23,24] As with *Staphylococcus aureus* USA300, the growth of *Corynebacterium striatum* was considerably inhibited by phage-mimicking ANPs with increasing silver coating on the gold nanospheres (Fig. 4C). At the time of this publication, no bactericidal activity studies of AgNPs could be found for *Corynebacterium striatum* within the current literature for comparison to the antibacterial efficacy of our phage-mimicking ANPs.

3.2.5 Quantification of the broad-spectrum capability of the phage-mimicking ANPs. To quantify and compare the antibacterial efficacy of the phage-mimicking ANPs, the linear slopes of the log phases of all growth curves were calculated. Smaller slopes indicate enhanced inhibition of bacterial growth. To compare the growth-curves between bacteria from different treatment groups, the slopes of the bacteria exposed to phage-mimicking ANPs were at first subtracted from the slopes of the control sample and then normalized by the slopes of the control sample (bacteria growing in LB media only without phage-mimicking ANPs).[49] The control-normalized log phase slopes revealed the percentage of growth-inhibition (Tables 5–7). The duration of log-phase growth and the starting time of the log phase were also determined. All three parameters (log phase inhibition, log phase duration, and log phase start time) enabled us to identify if the effect of the antimicrobial NPs was dependent on NP size (45 nm or 130 nm), silver coverage (LS, MS, or HS), dosage (0.1 ml, 0.5 ml, 1 ml, and 2 ml), or a combination thereof. We were able to examine how these three factors influenced the antimicrobial efficacy of the phage-mimicking ANPs against *S. aureus* USA300 (Fig. 3) (Table 5). However, for *P. aeruginosa* FRD1 and *E. faecalis* growth curves were only able to be analyzed for the different dosages (0.1 ml, 0.5 ml, and 1 ml) of the MS variant of the phage-mimicking ANPs (Fig. 4A and B) (Table 6). Similarly, for *C. striatum*, we were only able to analyze growth curves for the 1 ml dosage of the different silver coverages (LS, MS, or HS) (Fig. 4C) (Table 7). We utilized the log phase inhibition of *S. aureus* USA300 exposed to phage-mimicking ANPs as a standard against which we compared the log phase inhibition of *P. aeruginosa* FRD1, *E. faecalis*, and *C. striatum* exposed to an equal dose of phage-mimicking ANPs and silver-coverage.

S. aureus USA300 demonstrated a dosage-dependent and a silver coverage dependent sensitivity to phage-mimicking ANPs as indicated by the increased log phase inhibition with increasing dosage and increasing Ag coverage (Table 5). There

Table 5 Dose and silver-coverage dependent antimicrobial effect of phage-mimicking ANPs against *S. aureus* USA300

Bacteria	NP diameter (nm)	Ag coverage	Dosage (ml)	Linear slope log phase (h^{-1})	% Log phase retardation w.r.t control	Log phase start (h)	Duration of log phase (h)
S. aureus USA300	45 nm	Zero	0	0.280	0%	2.1	4.5
		LS	1	0.190	32.3%	2.6	5.5
			2	0.118	57.8%	1.4	7.8
		MS	1	0.111	60.3%	1.3	11.3
			2	0.094	66.5%	1.4	10.4
		HS	1	0.074	73.6%	2.7	12.6
			2	0.043	84.7%	2.6	21.4
	130 nm	Zero	0	0.280	0%	2.1	4.5
		LS	1	0.177	36.8%	2.6	4.7
			2	0.129	53.8%	1.9	7.3
		MS	1	0.138	50.8%	2.0	8.5
			2	0.100	64.3%	1.9	9.3
		HS	1	0.105	62.5%	8.5	8.8
			2	0.028	90.1%	10.6	9.5

were no clear trends that would indicate whether there was a size-dependent enhancement of phage-mimicking ANPs' antimicrobial efficacy. The maximum log phase inhibition achieved was 84.7% for 2 ml of 45 nm SiO_2@Au@Ag HS and 90.1% for 2 ml of 130 nm SiO_2@Au@Ag HS. In the presence of 2 ml of 45 nm SiO_2@Au@Ag HS phage-mimicking ANPs, *S. aureus* USA300 reached the lag phase after ~22 h, which was delayed 4-fold in comparison to the control. This indicates that the HS variant of the 45 nm SiO_2@Au@Ag was the most effective in inhibiting the growth of *S. aureus* USA300.

E. faecalis exhibited the maximum sensitivity to the phage-mimicking ANPs (Table 6). The log phase inhibition of *E. faecalis* when exposed to 3 different dosages (0.1 ml, 0.5 ml, and 1 ml) of MS coated phage-mimicking ANPs showed the same dose-dependent inhibition as *S. aureus* USA300. In *E. faecalis* there was additionally a size dependency in the efficacy of the phage-mimicking ANPs. 1 ml of the smaller MS coated phage-mimicking ANPs (45 nm) was ~20% more efficient in inhibiting the log growth phase in comparison to 1 ml of the larger MS coated phage-mimicking ANPs (130 nm). *P. aeruginosa* FRD1 in comparison was the least sensitive to MS coated phage-mimicking ANPs. Although there was a dose-dependent and size-dependent inhibition of the log growth phase, the maximum log phase inhibition was only 21.2% for *P. aeruginosa* FRD1 in comparison to the 60.3% for *S. aureus* USA300 and 72.5% for *E. faecalis* for the same dose. These results suggest that the mucoid strain *P. aeruginosa* FRD1 is more adept in preventing the interaction of the structure-based phage-mimicking ANPs with the bacterial cell membrane and more resistant to such phage-mimicking ANP designs once they form a mucinous mass.

C. striatum exhibited a size-dependent susceptibility to the smaller diameter phage-mimicking ANPs, inducing a higher inhibition of the log phase growth (Table 7). However, there was no apparent dependence of *C. striatum* susceptibility to the silver coverage on the phage-mimicking ANPs. The percent log phase inhibitions in the presence of LS, MS, and HS variants of the phage-mimicking ANPs were less than 3% apart. But, with nearly 50% inhibition of the log phase growth of *C. striatum* in the presence of 1 ml of 45 nm phage-mimicking ANPs, it was clear that *C. striatum* along with *S. aureus* USA300 and *E. faecalis* were the most susceptible to the antimicrobial effect of our rationally designed phage-mimicking nanoparticles. *P. aeruginosa* FRD1 also exhibited a significant decrease in log phase growth and a 2-fold decrease in the duration of the log phase (Table 6).

The growth curve results confirm the broad-spectrum capability of our phage mimicking ANPs. Our tests also revealed a mucus-like secretion employed as a potential defense mechanism by the mucoid bacterial strain *P. aeruginosa* FRD1 to overcome our structure-based phage-mimicking ANPs. In future iterations of the phage-mimicking nanoparticles, design consideration will be given to include anti-mucogenic ligands on the phage-mimicking ANPs to test if that might improve the

Table 6 Dose-dependent antimicrobial effect of MS phage-mimicking ANPs

Bacteria	Phage-mimicking ANP core diameter (nm)	Ag coverage	Dosage (ml)	Linear slope log phase (h^{-1})	% Log phase retardation w.r.t control	Log phase start (h)	Duration of log phase (h)
S. aureus USA300	45 nm	MS	0	0.2798	0%	2.1	4.5
			1	0.1112	60.3%	1.3	11.3
			2	0.09373	66.5%	1.4	10.4
	130 nm	MS	0	0.2798	0%	2.1	4.5
			1	0.1376	50.8%	2.0	8.5
			2	0.0998	64.3%	1.9	9.3
P. aeruginosa FRD1	45 nm	MS	0	0.131	0%	3.8	9.4
			0.1	0.1268	3.2%	6.8	8.6
			0.5	0.1104	15.7%	5.4	6.7
			1	0.1032	21.2%	7.3	5.5
	130 nm	MS	0	0.131	0%	3.8	9.4
			0.1	0.1273	2.8%	6.1	7.9
			0.5	0.1229	6.2%	6.1	6.6
			1	0.1205	8.0%	8.1	4.6
E. faecalis	45 nm	MS	0	0.1394	0%	2.9	2.4
			0.1	0.0911	34.6%	2.0	3.9
			0.5	0.0522	62.6%	3.4	2.7
			1	0.0383	72.5%	6.0	3.4
	130 nm	MS	0	0.1394	0%	2.9	2.4
			0.1	0.1248	10.5%	2.7	2.0
			0.5	0.074	46.9%	3.4	3.2
			1	0.0634	54.5%	6.0	2.6
C. striatum	45 nm	MS	0	0.158	0%	3.3	6.7
			1	0.082	48.0%	10.6	12.2
	130 nm	MS	0	0.158	0%	3.3	6.7
			1	0.111	29.7%	11.3	7.4

Table 7 Ag coverage-dependent antimicrobial effect of phage-mimicking ANPs for 1 ml dosage

Bacteria	Phage-mimicking ANP core diameter (nm)	Ag coverage	Dosage (ml)	Linear slope log phase (h^{-1})	% Log phase retardation w.r.t control	Log phase start (h)	Duration of log phase (h)
S. aureus USA300	45 nm	Zero	0	0.280	0%	2.1	4.5
		LS	1	0.190	32.3%	2.6	5.5
		MS	1	0.111	60.3%	1.3	11.3
		HS	1	0.074	73.6%	2.7	12.6
	130 nm	Zero	0	0.280	0%	2.1	4.5
		LS	1	0.177	36.8%	2.6	4.7
		MS	1	0.138	50.8%	2.0	8.5
		HS	1	0.105	62.5%	8.5	8.8
C. striatum	45 nm	Zero	0	0.158	0%	3.3	6.7
		LS	1	0.086	45.3%	7.8	8.2
		MS	1	0.082	48.0%	10.6	12.2
		HS	1	0.082	48.0%	13.3	6.0
	130 nm	Zero	0	0.158	0%	3.3	6.7
		LS	1	0.113	28.2%	9.3	9.5
		MS	1	0.111	29.7%	11.3	7.4
		HS	1	0.108	31.7%	14.1	5.9

antibacterial effect against mucoid strains of pathogenic bacteria.

3.2.6 Rational design of phage-mimicking antibacterial nanoparticles. The results of the bacterial growth curves after exposure to phage-mimicking ANPs have validated the antibacterial potential of our phage-mimicking nanoparticle design. The smaller phage-mimicking ANPs (45 nm) with the high silver coverage had the maximum antibacterial effect. We rationally added antibacterial elements to our phage-mimicking nanoparticles by using toxicology data from the existing literature to increase the toxicity of phage-mimicking ANPs selectively to bacterial cells. From a bactericidal point of view, we chose Au/Ag nanospheres of <5 nm for our phage-mimicking ANPs since it has been demonstrated in the peer-reviewed literature that when AgNPs with average diameters of <5 nm, 10 nm, and 90 nm were tested against *Pseudomonas aeruginosa*, the <5 nm AgNPs were highly efficient in accumulating in the bacteria.[50] The bacteria interacted with <5 nm AgNPs for a duration 1.5 orders of magnitude longer (>40 minutes) as opposed to their interaction with >10 nm AgNPs where their defensive behavior was immediate.[50] At the same time, the phage-mimicking architecture of the phage-mimicking ANPs with Au/Ag nanospheres resulted in minimizing the concentration of Ag used by 100-fold in comparison to Ag concentrations employed in the existing literature.[48,51] The highest Ag concentration on our phage-mimicking nanoparticles that exhibited >50% bactericidal activity is less than 95 μg ml^{-1}, which is well below the LC_{50} (5 mg ml^{-1}) of ≤5 nm AgNPs.[48] Our phage-mimicking nanoparticles have also exhibited broad-spectrum antibacterial activity against all four bacterial strains (*S. aureus* USA300, *P. aeruginosa* FRD1, *E. faecalis*, and *C. striatum*), two of which belong to the ESKAPE group of pathogens. The ability to target ESKAPE pathogens makes our phage-mimicking nanoparticles a significant active ingredient for antibacterial formulations.

3.3 Mechanism of antibacterial activity

Several studies have confirmed that the bactericidal effect of AgNPs is due to their ability to efficiently bind and reduce disulfide (S–S) bridges on the bacterial cell membrane.[52,53] In the absence of S–S bridges, the electron transport across the membrane is disrupted, leading to interference with bacterial energetics and rise in reactive oxygen species (ROS) in the bacteria.[52,54–56] Our phage-mimicking ANPs have been designed to be 1/10th to 1/5th the size of the bacteria. Zeta-potential (ζ-potential) measurements of the amine-functionalized silica core confirmed the positive surface charge with the 130 nm silica core having double the surface charge compared to the 45 nm silica core. The ζ-potential of the 45 nm silica core was 10.2 ± 3.4 mV, and the ζ-potential of the 130 nm silica core was 20.1 ± 7.4 mV. Upon addition of the negatively charged nanospheres to form the patchy shell on the silica-cores, the ζ-potentials of the 45 nm silica core and the 130 nm silica core dropped to −6.16 ± 3.4 mV and −4.07 ± 5.0 mV. While the net ζ-potential of the phage-mimicking ANPs was negative, the ζ-potential range was near zero mV, like that of zwitterionic molecules.[57] The zwitterionic nature of the phage-mimicking ANPs implies that the negatively charged membrane of the bacteria will interact with the phage-mimicking ANPs for durations long enough to allow Au/Ag on the phage-mimicking ANPs to bind to cysteine residues on the bacterial membrane without any hindrance from charge–charge repulsion.[58,59]

We hypothesize that the chemisorption of thiols from cysteine residues onto multiple Au/Ag nanospheres will immobilize the phage-mimicking nanoparticles on the bacteria, eventually leading to the physical disruption of the bacterial cell membrane.[60] The bacteria might initially sense the phage-mimicking nanoparticles as ≤5 nm Au/Ag nanospheres and thereby are slow to initiate their defense mechanisms.[50] Dark-field imaging was used to track the localized surface plasmon resonance signal (LSPRS) from Au and Ag on the phage-

mimicking ANPs (Fig. 5) using established techniques.[50,61–63] The LSPRS of the phage-mimicking ANPs lies in the visible spectrum (blue to red).[64] Darkfield imaging confirmed that the SiO_2@Au@Ag HS NPs exhibited LSPRS colors of blue, green, yellow, orange, and red (Fig. 5A and B). Additionally, darkfield imaging confirmed that untreated *S. aureus* USA300 appeared spherical, as expected (Fig. 5C).[65] However, *S. aureus* USA300 treated with SiO_2@Au@Ag HS phage-mimicking ANPs exhibited elliptical morphology with a dense number of NPs associated with the bacteria as confirmed through darkfield imaging (Fig. 5D), which showed that the LSPR signal of the phage-mimicking ANPs was colocalized with the bacteria.

Untreated control samples of *S. aureus* USA 300 had an average diameter of 1.39 μm and an aspect ratio of 1 in all directions. Samples of *S. aureus* USA 300 exposed to SiO_2@Au@Ag HS phage-mimicking ANPs were elliptical and possessed a short axis and a long axis with an aspect ratio of 3.57. In bacteria exposed to phage-mimicking ANPs, the diameter along the short axis was 1.77 μm, and the diameter along the long axis was 6.30 μm. SiO_2@Au@Ag HS phage-mimicking ANPs were co-localized with the bacterial membrane as seen in the representative darkfield images in Fig. 5E. This provides strong support for our hypothesis that the phage-mimicking structure of our phage-mimicking ANPs allows them to structurally and chemically prolong their interaction with the bacterial membrane, thus interrupting bacterial cell division, which will ultimately lead to physical disruption and death of the bacteria, as evidenced initially by inhibition of bacterial growth in our growth curve studies (Fig. 3 and 4).

3.4 Biocompatibility with a human skin cell line

All ten synthesized nanoparticle variations (SiO_2, SiO_2@Au, SiO_2@Au@Ag LS, SiO_2@Au@Ag MS, and SiO_2@Au@Ag HS; 45 nm or 130 nm) are highly biocompatible with human skin cells (HaCaT) Fig. 6. Subsamples of the HaCaT cell line incubated with the nanoparticles for 16 h showed growth and a healthy appearance of the cells (Fig. 6B and C).

In general, the use of silica-based materials is not considered harmful to humans.[66] Depending on the size and concentration as well as the exposure/drug delivery routes in tested cell lines, silica nanoparticles cover a wide spectrum between biocompatible and slightly toxic.[66] But nonporous amorphous silica NPs (>10 nm) with APTES molecules, similar to the ones employed as cores in our phage-mimicking ANPs, have proven biocompatibility with human cells (*e.g.*, Calu-3).[67] Silver nanoparticles have also been recommended as a good alternative for the control of

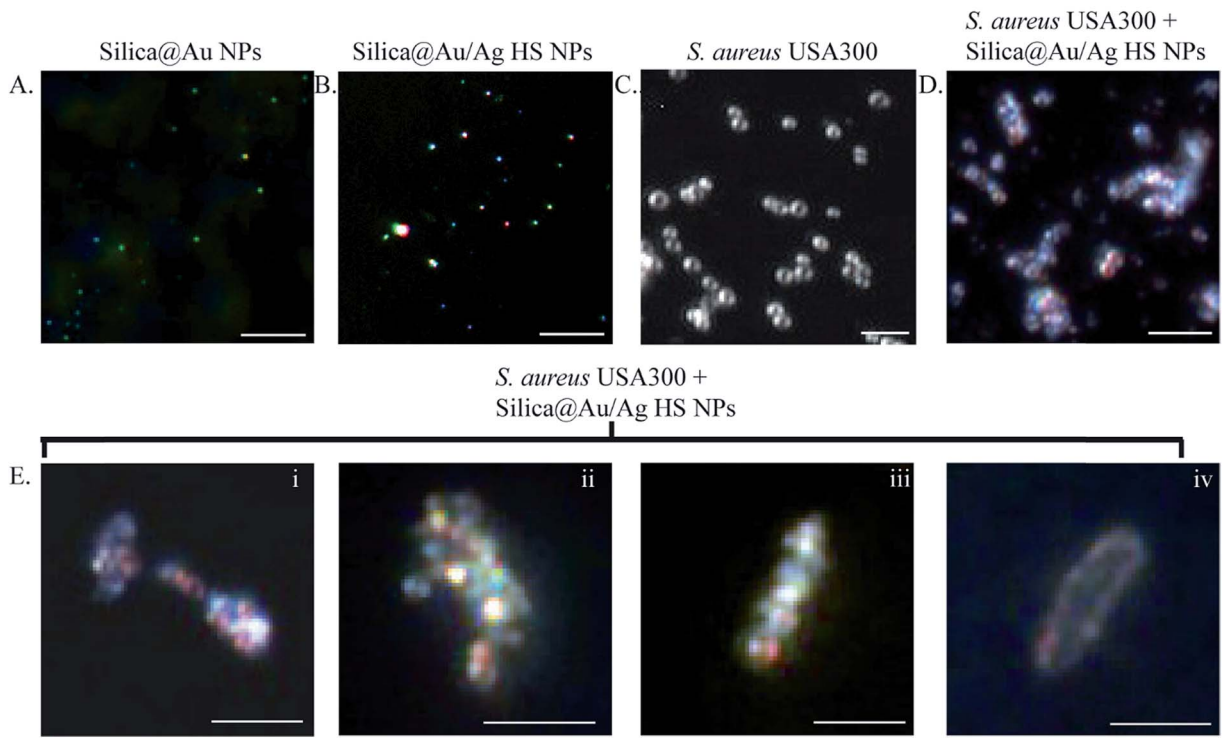

Fig. 5 Darkfield microscopy was used to assess the effect of the phage-mimicking nanoparticle treatment on the morphology of *S. aureus* USA300. (A) Darkfield images of the localized surface plasmon resonance (LSPR) of Au nanoclusters on the 45 nm silica cores. The LSPRS of Au was either green or orange, which is in good accordance with the existing literature. (B) The LSPRS of high silver-coated Au nanoclusters on the 45 nm silica core was a rainbow of colors with blue, green, yellow, and red being prominent. (C) Darkfield images showed that untreated *S. aureus* USA300 appeared spherical. (D) However, *S. aureus* USA300 treated with SiO_2@Au@Ag HS phage-mimicking ANPs exhibited elliptical morphology with a high density of the NPs associated with the bacteria as confirmed through dark-field imaging of the bacteria as well as the LSPR signal of NPs from the bacteria. (E) Magnified images of elliptical *S. aureus* USA300 with the characteristic LSPR signal of silver on SiO_2@Au@Ag HS phage-mimicking ANPs. Scale bars are all 10 μm. The LSPR images of the nanoparticles are all diffraction-limited and not the actual size of the nanoparticles.

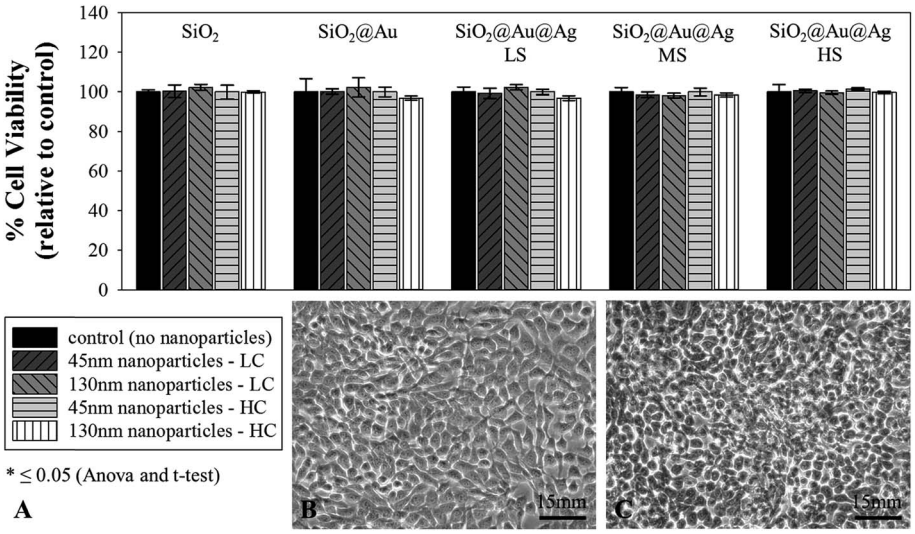

Fig. 6 (A) Cell viability (% of control) for all ten synthesized NP variations: SiO_2, SiO_2@Au, SiO_2@Au@Ag LS (low silver), SiO_2@Au@Ag MS (medium silver), and SiO_2@Au@Ag HS (high silver), with both 45 and 130 nm SiO_2 cores, and at two concentrations (low concentration and high concentration). LC, low concentration = approximately 6.99×10^{11} particles per ml of 45 nm phage-mimicking ANPs and 1.09×10^{11} particles per ml of 130 nm phage-mimicking ANPs; HC, high concentration = approximately 1.40×10^{12} particles per ml of 45 nm phage-mimicking ANPs and 2.19×10^{11} particles per ml of 130 nm phage-mimicking ANPs. Optical microscope images showing (B) HaCaT cells in DMEM and (C) after treatment with 45 nm NPs with HS coating.

bacterial strains, with less risk of toxicity to mammalian cells.[68] But silver nanoparticle toxicity to eukaryotic cells is size-dependent. Using data from dose-dependent toxicity studies of AgNPs to eukaryotic cells, we extrapolated the size- and shape-dependent toxicity of nanomaterials.[69] The LC_{50} of AgNPs ≤10 nm (1180 ± 140 μg ml^{-1}) against eukaryotic fibroblast cells is lower than that of AgNPs >10 nm (1760 ± 110 μg ml^{-1}) since the smaller AgNPs are easily taken up by cells and concentrated intracellularly, much more than the >10 nm AgNPs.[51]

Despite choosing Au/Ag nanospheres <5 nm for our phage-mimicking ANPs, we hypothesize that the lack of abundance of cysteine residues on eukaryotic cell membranes, the zwitterionic nature of the nanoparticles (similar to PEG-coated nanoparticles) as determined from zeta potential measurements, the ~10-fold increase in the effective diameter of the immobilized Au/Ag nanospheres on the silica cores, and the size of the eukaryotic cells still being ~200-fold larger than the phage-mimicking ANPs, will increase the repulsion of our phage-mimicking nanoparticles away from the surface of eukaryotic cells.[51] The arrangement of the <5 nm Au/Ag nanospheres on a >45 nm silica core also ensures that the Au/Ag nanospheres do not present themselves as ≤5 nm AgNPs, thereby reducing the probability of the phage-mimicking ANPs permeabilizing the eukaryotic cell membrane. The phage-mimicking structure of our ANPs increased the biocompatibility towards eukaryotic cells as was evident from our tests on model skin cell lines (HaCaT).[66] Additionally, the Environmental Protection Agency (EPA) has established a chronic oral Reference Dose (RfD) of 5 μg per kg per day for silver which broadly translates to 250 μg to 750 μg per person per day.[48] Our phage-mimicking ANPs exhibit a maximum silver content of 189.22 μg ml^{-1} and a predicted amount of <1 μg ml^{-1} silver ions leaching into solution which are well below the EPA prescribed safety limits for exposure to silver.

4. Conclusions

Rational nanoparticle engineering revealed that the previously hypothetical phage-mimicking nanoparticles could be synthesized with very specific properties (bactericidal, biocompatible, *etc.*). The structural approach and the modular assembly of the nanoparticles designed by our lab are effective against four different nosocomial strains (*Staphylococcus aureus* USA300, *Pseudomonas aeruginosa* FRD1, *Corynebacterium striatum*, and *Enterococcus faecalis*), strongly inhibiting and suppressing their growth. All four strains grow slower (inhibition of log-phase growth) and do not reach their maximal growth potential (optical density@600 nm cut down by approximately 1/2 to 1/3 compared to nanoparticle-free growth). Growth inhibition is dependent on the silver coating concentration on the gold nanospheres, with a higher silver concentration positively correlated with higher bactericidal and increased antibacterial efficacy of the nanoparticles. However, the bactericidal properties of our phage-mimicking ANPs were not a function of Ag concentration alone. Previously existing literature that has utilized AgNPs in the size range of 8–100 nm demonstrated that bacterial defenses (*P. aeruginosa* and *B. subtilis*) were highly efficient in the efflux of individual AgNPs.[50] To confirm the importance of our structure-based antibacterial design approach, phage-mimicking ANPs were tracked using the signal from the LSPR of Au/Ag nanoclusters in dark-field imaging to conclusively demonstrate that our phage-mimicking ANPs, much like their biological counterparts, remain irreversibly associated with the bacterial cell wall. The phage-mimicking

ANPs bound to the bacterial membranes played a disruptive role during multiple bacterial divisions resulting in an abnormally elongated morphology being exhibited by *S. aureus* USA300. Phage-mimicking ANPs induced a dose-dependent 21% to 90% log phase inhibition when tested against the four different nosocomial bacterial strains. In addition to the phage-mimicking ANPs' advantageous bacteriostatic activity, the inorganic phage-mimicking nanoparticles are also biocompatible with human skin cells. Our phage-mimicking ANPs are the first to demonstrate an antibacterial activity that is dependent on the structure of the NPs, resulting in a bactericidal activity that is greater than that of the sum of the individual components that constitute the nanoparticles. Our results demonstrate an innovative and proactive approach to deal with the rising threat of antibiotic-resistant bacteria. Our robust, modularly assembled, antibacterial NPs can be applied to infectible surfaces to pre-empt an infection from even developing at the tissue/material interface. This study where we employed modular assembly to engineer our phage-mimicking ANPs hierarchically and to gain a clearer understanding of the component-to-structure-to-function relationship has laid the foundation for future structure-based, antibiotic-free antibacterial nanoparticles with higher bactericidal efficiency and bacterial specificity to stem the continued rise of antibiotic-resistant strains of bacteria.

Conflicts of interest

There are no conflicts of interests to declare.

Acknowledgements

The Nallathamby lab would like to acknowledge the financial and material support of the Notre Dame Center for Nano Science and Technology (NDnano) and the Notre Dame Center for Advanced Diagnostics and Therapeutics (AD&T). Dr Nallathamby's research was supported by a Project Development Team grant from the Indiana Clinical and Translational Sciences Institute (CTSI-PDT: 373037-31005-FY19CTSIK), an Institutional Research Grant from the American Cancer Society (ACS IRG-17-182-04) and a seed grant from the Notre Dame Advanced Diagnostics and Therapeutics Center (372333-31025). Dr Hopf's research was supported by a grant from the Advanced Diagnostics and Therapeutics research initiative at the University of Notre Dame (372717-43310-FY17RFP). Margo Waters was funded through an NDnano Undergraduate Research Fellowship (NURF) and Veronica Kalwajtys was funded through a College of Science-Summer Undergraduate Research Fellowship (COS-SURF).

References

1 C. L. Ventola, *Pharm. Therapeut.*, 2015, **40**, 277–283.
2 S. Santajit and N. Indrawattana, *BioMed Res. Int.*, 2016, **2016**, 2475067.
3 J. N. Pendleton, S. P. Gorman and B. F. Gilmore, *Expert Rev. Anti-Infect. Ther.*, 2013, **11**, 297–308.
4 D. Pletzer, S. C. Mansour, K. Wuerth, N. Rahanjam and R. E. Hancock, *mBio*, 2017, **8**, e00140.
5 L. L. Silver, *Clin. Microbiol. Rev.*, 2011, **24**, 71–109.
6 L. O'Neill, *Vet. Rec.*, 2016, **178**, 590.
7 S. B. Zaman, M. A. Hussain, R. Nye, V. Mehta, K. T. Mamun and N. Hossain, *Cureus*, 2017, **9**, e1403.
8 H. A. Hemeg, *Int. J. Nanomed.*, 2017, **12**, 8211–8225.
9 N. Beyth, Y. Houri-Haddad, A. Domb, W. Khan and R. Hazan, *J. Evidence-Based Complementary Altern. Med.*, 2015, **2015**, 246012.
10 A. Gupta, R. F. Landis and V. M. Rotello, *F1000Research*, 2016, **5**, 1–10.
11 R. Y. Pelgrift and A. J. Friedman, *Adv. Drug Delivery Rev.*, 2013, **65**, 1803–1815.
12 A. J. Huh and Y. J. Kwon, *J. Controlled Release*, 2011, **156**, 128–145.
13 R. P. Allaker and G. Ren, *Trans. R. Soc. Trop. Med. Hyg.*, 2008, **102**, 1–2.
14 B. Ramalingam, T. Parandhaman and S. K. Das, *ACS Appl. Mater. Interfaces*, 2016, **8**, 4963–4976.
15 P. V. Baptista, M. P. McCusker, A. Carvalho, D. A. Ferreira, N. M. Mohan, M. Martins and A. R. Fernandes, *Front. Microbiol.*, 2018, **9**, 1441.
16 A. Sirelkhatim, S. Mahmud, A. Seeni, N. H. M. Kaus, L. C. Ann, S. K. M. Bakhori, H. Hasan and D. Mohamad, *Nano-Micro Lett.*, 2015, **7**, 219–242.
17 S. Pal, Y. K. Tak and J. M. Song, *Appl. Environ. Microbiol.*, 2007, **73**, 1712–1720.
18 N. G. Bonine, A. Berger, A. Altincatal, R. Wang, T. Bhagnani, P. Gillard and T. Lodise, *Am. J. Med. Sci.*, 2019, **357**, 103–110.
19 E. M. Windels, J. E. Michiels, M. Fauvart, T. Wenseleers, B. Van den Bergh and J. Michiels, *ISME J.*, 2019, **13**, 1239–1251.
20 H. W. Ackermann, *Adv. Virus Res.*, 1998, **51**, 135–201.
21 E. B. Gordon, C. J. Knuff and B. A. Fane, *J. Virol.*, 2012, **86**, 9911–9918.
22 F. C. Tenover and R. V. Goering, *J. Antimicrob. Chemother.*, 2009, **64**, 441–446.
23 A. Neemuchwala, D. Soares, V. Ravirajan, A. Marchand-Austin, J. V. Kus and S. N. Patel, *Antimicrob. Agents Chemother.*, 2018, **62**, e01776.
24 A. A. Weaver, N. A. Hasan, M. Klaassen, H. Karathia, R. R. Colwell and J. D. Shrout, *J. Med. Microbiol.*, 2019, **68**, 1507–1516.
25 G. Ryan, T. Dolling and S. Barnet, *Med. Educ.*, 2004, **38**, 638–645.
26 D. E. Ohman and A. M. Chakrabarty, *Infect. Immun.*, 1981, **33**, 142–148.
27 W. Wang, P. D. Nallathamby, C. M. Foster, J. L. Morrell-Falvey, N. P. Mortensen, M. J. Doktycz, B. Gu and S. T. Retterer, *Nanoscale*, 2013, **5**, 10369–10375.
28 T. H. L. Nghiem, T. N. Le, T. H. Do, T. T. D. Vu, Q. H. Do and H. N. Tran, *J. Nanopart. Res.*, 2013, **15**, 2091.
29 P. Manivel, A. Balamurugan, N. Ponpandian, D. Mangalaraj and C. Viswanathan, *Spectrochim. Acta, Part A*, 2012, **95**, 305–309.

30 J. M. Laing, M. D. Gober, E. K. Golembewski, S. M. Thompson, K. A. Gyure, P. J. Yarowsky and L. Aurelian, *Mol. Ther.*, 2006, **13**, 870–881.
31 F. Fenner, *Virology*, 1976, **71**, 371–378.
32 M. Takac, A. Witte and U. Blasi, *Microbiology*, 2005, **151**, 2331–2342.
33 P. R. Chipman, M. Agbandje-McKenna, J. Renaudin, T. S. Baker and R. McKenna, *Structure*, 1998, **6**, 135–145.
34 P. Willingmann, S. Krishnaswamy, R. McKenna, T. J. Smith, N. H. Olson, M. G. Rossmann, P. L. Stow and N. L. Incardona, *J. Mol. Biol.*, 1990, **212**, 345–350.
35 K. L. Brentlinger, S. Hafenstein, C. R. Novak, B. A. Fane, R. Borgon, R. McKenna and M. Agbandje-McKenna, *J. Bacteriol.*, 2002, **184**, 1089–1094.
36 S. R. Bhattarai, S. Y. Yoo, S. W. Lee and D. Dean, *Biomaterials*, 2012, **33**, 5166–5174.
37 J. Ren, Y. Guo, L. Shao, Y. Liu and Q. Liu, *Exp. Ther. Med.*, 2018, **16**, 3286–3292.
38 S. Wei, Q. Liu, T. Lian and L. Shao, *Virus Res.*, 2019, **267**, 1–8.
39 J. Sliwa-Dominiak, E. Suszynska, M. Pawlikowska and W. Deptula, *Arch. Microbiol.*, 2013, **195**, 765–771.
40 T. D. Read, C. M. Fraser, R. C. Hsia and P. M. Bavoil, *Microb. Comp. Genomics*, 2000, **5**, 223–231.
41 S. Fischer, J. K. Swabeck and A. P. Alivisatos, *J. Am. Chem. Soc.*, 2017, **139**, 12325–12332.
42 E. Z. Gomaa, *J. Genet. Eng. Biotechnol.*, 2017, **15**, 49–57.
43 E. Z. Gomaa, *J. Gen. Appl. Microbiol.*, 2017, **63**, 36–43.
44 D. P. Tamboli and D. S. Lee, *J. Hazard. Mater.*, 2013, **260**, 878–884.
45 G. A. Sotiriou, G. D. Etterlin, A. Spyrogianni, F. Krumeich, J. C. Leroux and S. E. Pratsinis, *Chem. Commun.*, 2014, **50**, 13559–13562.
46 M. Hentzer, G. M. Teitzel, G. J. Balzer, A. Heydorn, S. Molin, M. Givskov and M. R. Parsek, *J. Bacteriol.*, 2001, **183**, 5395–5401.
47 X. Yan, B. He, L. Liu, G. Qu, J. Shi, L. Hu and G. Jiang, *Metallomics*, 2018, **10**, 557–564.
48 R. Krishnan, V. Arumugam and S. K. Vasaviah, *J. Nanomed. Nanotechnol.*, 2015, **6**, 4.
49 R. P. Smith, A. L. Baltch, P. B. Michelsen, W. J. Ritz and R. Alteri, *Antimicrob. Agents Chemother.*, 2003, **47**, 1081–1087.
50 P. D. Nallathamby, K. J. Lee, T. Desai and X. H. Xu, *Biochemistry*, 2010, **49**, 5942–5953.
51 A. Ivask, I. Kurvet, K. Kasemets, I. Blinova, V. Aruoja, S. Suppi, H. Vija, A. Kakinen, T. Titma, M. Heinlaan, M. Visnapuu, D. Koller, V. Kisand and A. Kahru, *PLoS One*, 2014, **9**, e102108.
52 W. K. Jung, H. C. Koo, K. W. Kim, S. Shin, S. H. Kim and Y. H. Park, *Appl. Environ. Microbiol.*, 2008, **74**, 2171–2178.
53 W. K. Jung, H. C. Koo, K. W. Kim, S. Shin, S. H. Kim and Y. H. Park, *Appl. Environ. Microbiol.*, 2008, **74**, 2171–2178.
54 O. Gordon, T. Vig Slenters, P. S. Brunetto, A. E. Villaruz, D. E. Sturdevant, M. Otto, R. Landmann and K. M. Fromm, *Antimicrob. Agents Chemother.*, 2010, **54**, 4208–4218.
55 M. Akter, M. T. Sikder, M. M. Rahman, A. Ullah, K. F. B. Hossain, S. Banik, T. Hosokawa, T. Saito and M. Kurasaki, *J. Adv. Res.*, 2018, **9**, 1–16.
56 H. L. Su, C. C. Chou, D. J. Hung, S. H. Lin, I. C. Pao, J. H. Lin, F. L. Huang, R. X. Dong and J. J. Lin, *Biomaterials*, 2009, **30**, 5979–5987.
57 W. Wang, Y. Lu, Z. Yue, W. Liu and Z. Cao, *Chem. Commun.*, 2014, **50**, 15030–15033.
58 M. E. Bayer and J. L. Sloyer Jr, *J. Gen. Microbiol.*, 1990, **136**, 867–874.
59 H. Ou, T. Cheng, Y. Zhang, J. Liu, Y. Ding, J. Zhen, W. Shen, Y. Xu, W. Yang, P. Niu, J. Liu, Y. An, Y. Liu and L. Shi, *Acta Biomater.*, 2018, **65**, 339–348.
60 E. Pensa, E. Cortés, G. Corthey, P. Carro, C. Vericat, M. H. Fonticelli, G. Benítez, A. A. Rubert and R. C. Salvarezza, *Acc. Chem. Res.*, 2012, **45**, 1183–1192.
61 K. J. Lee, L. M. Browning, T. Huang, F. Ding, P. D. Nallathamby and X. H. Xu, *Anal. Bioanal. Chem.*, 2010, **397**, 3317–3328.
62 P. D. Nallathamby and X. H. Xu, *Nanoscale*, 2010, **2**, 942–952.
63 T. Huang, P. D. Nallathamby, D. Gillet and X. H. Xu, *Anal. Chem.*, 2007, **79**, 7708–7718.
64 P. D. Nallathamby, T. Huang and X. H. Xu, *Nanoscale*, 2010, **2**, 1715–1722.
65 B. K. Monson, J. Stringham, B. B. Jones, S. Abdel-Aziz, C. M. Cutler Peck and R. J. Olson, *J. Ocul. Pharmacol. Ther.*, 2010, **26**, 133–136.
66 H. Jaganathan and B. Godin, *Adv. Drug Delivery Rev.*, 2012, **64**, 1800–1819.
67 J. McCarthy, I. Inkielewicz-Stepniak, J. J. Corbalan and M. W. Radomski, *Chem. Res. Toxicol.*, 2012, **25**, 2227–2235.
68 R. Salomoni, P. Leo, A. F. Montemor, B. G. Rinaldi and M. Rodrigues, *Nanotechnol., Sci. Appl.*, 2017, **10**, 115–121.
69 W. Liu, Y. Wu, C. Wang, H. C. Li, T. Wang, C. Y. Liao, L. Cui, Q. F. Zhou, B. Yan and G. B. Jiang, *Nanotoxicology*, 2010, **4**, 319–330.
70 L. L. Ilang, N. H. Olson, T. Dokland, C. L. Music, R. H. Cheng, Z. Bowen, R. McKenna, M. G. Rossmann, T. S. Baker and N. L. Incardona, *Structure*, 1995, **3**, 353–363.